Journal of the European Ceramic Society 45 (2025) 117588

Contents lists available at ScienceDirect

Journal of the European Ceramic Society

journal homepage: www.elsevier.com/locate/jeurceramsoc

# The impact of $SrTiO_3$, $CaTiO_3$ and $BaTiO_3$ on the formation of core-shell structures in solid solutions with $Na_{0.5}Bi_{0.5}TiO_3$

Sophie Bauer [a,*], Marc Widenmeyer [a], Till Frömling [b]

[a] Technical University of Darmstadt, Department of Materials and Earth Science, Peter-Grünberg-Straße 2, Darmstadt 64287, Germany
[b] Forschungszentrum Jülich GmbH, Institute of Energy Technologies (IET), Wilhelm-Johnen-Straße, Jülich 52428, Germany

ARTICLE INFO

*Keywords:*
Lead-free
Bismuth titanates
Core-shell
Relaxor
Electromechanical properties
Impedance

ABSTRACT

The solid solution $75Na_{0.5}Bi_{0.5}TiO_3$-$25SrTiO_3$ (NBT-ST) can achieve outstanding high-strain properties for actuator applications. Whether these properties arise from microscopic core-shell structures or coexisting polar nanoregions remains uncertain, thus opening up a promising research field for tuning functional properties. One possible way to reveal the underlying core-shell formation mechanism and the structure's impact on functional properties is to test related solid solutions with NBT. This study examines the applicability of core-shell formation conditions and associated property changes in NBT-ST to $87Na_{0.5}Bi_{0.5}TiO_3$ $-13CaTiO_3$ (NBT-CT) and $94Na_{0.5}Bi_{0.5}TiO_3$–$6BaTiO_3$ (NBT-BT). Thermal analysis and scanning electron microscopy revealed that two-step reactions, as in NBT-ST and NBT-CT, are the key factor enabling core-shell structures. A single-step reaction, like in NBT-BT resulted in no core-shell structures. As already demonstrated for NBT-ST, core-shell structures in NBT-CT led to comparably high strains of 0.29 % and slim polarisation loops, confirming the transferability of property changes associated with chemical inhomogeneities.

## 1. Introduction

Lead-free piezoelectric ceramics have attracted considerable attention over the past decade, driven by increasing environmental and health concerns associated with the widely used lead-based materials like lead zirconate titanate (short PZT) [1,2]. $BaTiO_3$-based (BT-based), $(K,Na)NbO_3$-based (KNN-based), and $Na_{0.5}Bi_{0.5}TiO_3$-based (NBT-based) piezoelectric materials have demonstrated promising functional properties, often comparable or even exceeding those of their lead-based counterparts [3–6]. Referring to the lead-free KNN-based [7–9] and NBT-based [10–15] ceramics, significant changes within the ferroelectric and electric properties due to chemical inhomogeneities have been shown in literature. Especially, the solid solution of $SrTiO_3$ (ST) and NBT (short NBT-ST) is of particular interest as the material system exhibits excellent high-strain properties fulfilling the requirements of actuator applications [11,15–21]. Investigations into these exceptional strain properties revealed that chemical inhomogeneities form as core-shell structures during the conventional solid-state sintering process [10,11,13]. Koruza et al. [10] demonstrated that the formation of core-shell structures is strongly influenced by the calcination process that occurs in two stages. The NBT reacts at temperatures approximately 200 °C lower than required to form ST. Apart from that, the sintering conditions, such as dwell time and temperature, have a significant impact as the $Sr^{2+}$ partially diffuses into the already-formed NBT network during the sintering process [14]. Additionally, the concentration of oxygen vacancies plays a key role in the core-shell formation and can, for example, be controlled by the bismuth content of the sample (Eq. (1)).

$$2Bi_2O_3 + 2V_{Bi}''' + 3V_O^{\bullet\bullet} \rightarrow 2Bi_{Bi}^{x} + O_O^{x} \tag{1}$$

Eq. (1) demonstrates that a higher Bi content in the sample results in a lower concentration of oxygen vacancies. For NBT-ST, it was hypothesised that this suppresses the chemical diffusion of $Sr^{2+}$ and $O^{2-}$ required to achieve chemical homogeneity. As a result, the probability of forming chemical heterogeneities, like core-shell structures, is significantly increased [10,13,14]. Although recent research suggests that the remarkable strain properties arise from a reversible field-induced ferroelectric phase transition of the ferroelectric NBT core from a polar to a non-polar phase [11,13,14,22], alternative explanations, such as different coexisting nanoscale inhomogeneities like polar nanoregions, cannot be excluded [23–25]. Nevertheless, the substantial impact of chemical inhomogeneities on material properties, particularly in enabling an advantageous tuning of the material's properties, remains

---

* Corresponding author.
*E-mail address:* sophie.bauer@mr.tu-darmstadt.de (S. Bauer).

https://doi.org/10.1016/j.jeurceramsoc.2025.117588
Received 13 March 2025; Received in revised form 19 May 2025; Accepted 1 June 2025

undeniable. Therefore, it is of great interest to gain a deeper understanding of the conditions governing the chemical inhomogeneities – such as a two-step formation process, precise control of sintering parameters as well as the reduction of oxygen vacancies – and to explore their formation in other solid solutions. While there is evidence of inhomogeneities in form of core-shell structures in NBT-ST, similar indications based on electromechanical properties have been observed in solid solutions of NBT with $CaTiO_3$ [26], $BaZrO_3$ [27], and $SrZrO_3$ [28]. However, a direct observation has not yet been achieved. In contrast, no instance of core-shell formation has been found in the solid solution of NBT and $BaTiO_3$ [29]. In order to gain a better understanding of the formation processes, driving forces, and reaction pathways of other solid solutions, $CaTiO_3$ (CT) and $BaTiO_3$ (BT) were selected for this study. These systems are particularly intriguing, as they may behave similarly to the reference material system NBT-ST. $Ca^{2+}$, $Sr^{2+}$, and $Ba^{2+}$ ions share the same valence, have comparable electronegativities, and occupy the *A*-site of a perovskite unit cell [30,31]. Understanding whether the electromechanical property trends observed in NBT-CT, as reported in previous studies [26], can be correlated with a core shell microstructure and why no such indications could be found for NBT-BT [29], will provide valuable insights into the fundamental requirements and driving forces for the core-shell formation. Since compositions located at the morphotropic-phase-boundary (MPB) are known to exhibit enhanced properties [19], NBT-6BT [32], [33] and NBT-13CT [34–36] are compared with the reference composition NBT-25ST [37–39]. However, optimising the material behaviour by, for example, controlling the concentration of core-shell structures, lies beyond the scope of this work and needs to be addressed in the future.

The aim of this work is to systematically investigate the formation of NBT in solid solutions with the titanates BT, CT, or ST and to evaluate their effect on the ferroelectric and electrical properties. First, the formation mechanisms of each solid solution are analysed and correlated with the microstructural development, particularly focusing on whether core-shell structures are formed. In this context, it is of particular interest to determine whether a similar influence of the oxygen vacancy concentration, as observed in NBT-ST, can be demonstrated in the other material systems. This would allow for the identification of key requirements for controlling the core-shell formation. Second, the impact of the different solid solutions on ferroelectric and electrical properties is studied, with particular emphasis on linking the microstructure to the functional properties. Combining the formulation of key requirements for the core–shell formation with a correlation between microstructure and certain material properties will contribute to the development of targeted strategies for tailoring future functional materials.

## 2. Experimental procedure

Bulk ceramics were prepared via the solid-state synthesis route by using $Na_2CO_3$ (99.5 %), $Bi_2O_3$ (99.975 %), $TiO_2$ (anatase: 99.6 %), $SrCO_3$ (99.9 %), $CaCO_3$ (99.5 %), and $BaCO_3$ (99.8 %) *(all from: Alfa Aesar GmbH & Co, KG, Germany)*. Before weighing the raw powders, a drying step for $Na_2CO_3$ (300 °C), $Bi_2O_3$ (180 °C), $TiO_2$ (800 °C), $SrCO_3$ (180 °C), $CaCO_3$ (180 °C), and $BaCO_3$ (180 °C) was carried out for 8 h. All dried powders were weighed according to the stoichiometric formulas $75Na_{0.5}Bi_xTiO_3$–$25SrTiO_3$ (NBT-ST), $87Na_{0.5}Bi_xTiO_3$–$13CaTiO_3$ (NBT-CT), and $94Na_{0.5}Bi_xTiO_3$–$6BaTiO_3$ (NBT-BT) with $x = 0.495$, 0.5, 0.505. The milling of all raw powders of the different compositions was executed by using nylon milling containers with yttria-stabilised zirconia balls (diameter: 10 mm; ratio: 10:1) and ethanol in a planetary ball mill *(Fritsch Pulverisette 5, Germany)* for 24 h at 250 rpm. The suspensions of the milled powders were dried at 100 °C for 24 h and afterwards calcined at 750 °C for 2 h. Subsequently, the calcined powders were wet milled with ethanol in a planetary ball mill for 24 h at 250 rpm and dried at 100 °C for 24 h. The second calcination was performed at 850 °C for 2 h followed by a final wet milling step with ethanol for 24 h at 250 rpm and drying step at 100 °C for 24 h. Disk shaped pellets with a diameter of 10 mm and ~ 0.3 g were obtained by uniaxially pressing at 25 MPa and additional cold isostatic pressing at 350 MPa *(P.O. Weber KIP 100 E, Germany)*. The green bodies were covered with sacrificial powder and sintered in alumina crucibles at 1150 °C for 2 h using a heating rate of 5 K/min. The density of the sintered pellets was determined by the Archimedes principle. As all densities turned out to be larger than 95 %, the samples were considered dense enough for further electrical and ferroelectric characterisations.

In order to investigate the calcination behaviour, homogenised and stoichiometric mixtures of each composition were analysed by thermogravimetric analysis (TGA), differential thermal analysis (DTA), and evolved gas analysis (EGA) using mass spectroscopy. Approximately 67 mg to 100 mg of each mixture was weighed in an alumina crucible and placed in a STA449C Jupiter *(Netzsch Gerätebau GmbH, Germany)* for TGA/DTA. For EGA a QMS403C Aëolos mass spectrometer *(Netzsch Gerätebau GmbH, Germany)* coupled directly to the STA with a heated transfer line operated at 200 °C was used. The following mass-to-charge signals (*m/z*) were analysed as quasi multi-ion detection (QMID): $m/z = 12$ ($C^+$), 18 ($H_2O^+$), and 44 ($CO_2^+$). The measurements were carried out with a heating rate of 5 K/min up to 1000 °C in flowing synthetic air at a rate of 60 ml/min and 8 ml/min argon as protective gas. All measurements were corrected for buoyancy.

To prepare the samples for the (micro-)structural analysis, the samples were ground and polished down to ¼ μm.

For the validation of the phase purity, the sintered and polished pellets were examined by X-ray diffraction (XRD) *(Cu $K_{\alpha 1}/K_{\alpha 2}$; AXS D8, Bruker Corporation, Germany)*. The microstructure of each sample was visualised with back-scattered electrons (BSE) at 15 kV using a scanning electron microscope (SEM) TESCAN MIRA 3 *(TESCAN, Czech Republic)* with a beam intensity of 10. In addition, the grain size was determined from the SEM images using the software LINCE V 2.4.2. *(Sergio Luis dos Santos e Lucato, NAW, TU Darmstadt, Germany)* considering about 200 grains.

For conducting the large signal electrical measurements such as polarisation and strain curves, the samples were ground with a 47 μm grinding wheel and sputtered with Ag electrodes (full sample area with approx. diameter of 7.7 mm and height around 0.5 mm). A bipolar triangular wave and 1 Hz was chosen as an input signal *(20/20 C, TREK Inc., USA)* when executing the measurements with a conventional Sawyer–Tower (reference capacitor $C_{\text{ref}} = 15$ μF) setup combined with an optical strain sensor *(Philtec Inc., USA)*.

Regarding the small signal electrical measurements such as impedance spectroscopy and permittivity measurements another set of samples was sputtered with Pt electrodes (full sample area with approx. diameter of 7.7 mm and height around 0.5 mm). Impedance spectroscopy was carried out with an Alpha-A High-Performance Frequency Analyser *(Novocontrol Technologies, Germany)* at different temperatures (150 °C-600 °C, 25 °C steps, and heating rate of 5 K/min). The amplitude was 0.1 V and the frequency range was 0.1 Hz to 3 MHz. All spectra were analysed with the RelaxIS software *(RHD instruments, Germany)*. Temperature and frequency dependent dielectric permittivity and tan($\delta$) measurements have been executed using a 4284 A Precision LCR-Meter *(Hewlett Packard, USA)* connected to a conventional box furnace using the 4-point set-up. During each experiment data were acquired for 100 Hz, 1 kHz, 10 kHz, 100 kHz and 1 MHz for temperatures ranging from 25 °C to 450 °C.

## 3. Results and discussion

### 3.1. Formation of core-shell microstructures

A combined TGA/DTA/EGA analysis has proven to be an effective method for understanding the calcination behaviour and reaction pathways in the reference system NBT-ST [10]. Some initial conclusions about the underlying mechanisms for the core-shell formation have already been drawn, as their findings revealed a two-step reaction, with

NBT forming first at around 590 °C, followed by ST at approximately 800 °C. This decoupling of both reactions occurs due to different onset temperatures for the NBT and ST formation. The raw components of NBT begin forming a first perovskite phase at 530 °C [40], while the ST phase starts to develop at 800 °C [41]. Building on this preliminary study, additional TGA, DTA and EGA measurements were conducted to investigate the reaction pathways of NBT-CT and NBT-BT and determine whether core-shell structures are likely to also form in these systems. To identify the different reaction stages, Fig. 1 presents the temperature dependent measurements of homogenised and stoichiometric mixtures of the starting powders for the MPB compositions of NBT-13CT [34–36] and NBT-6BT [32,33] during heating. To account for variations appearing due to the differences in CT, and BT contents, another set of measurements was performed on stoichiometric mixtures of the starting powders of NBT-25CT and NBT-25BT (supplementary material Figure S1).

The TGA/DTA and EGA results show multiple processes. The endothermic peak at 100 °C represents the evaporation of residual $H_2O$ in all samples. In addition, small exothermic peaks at 250 °C-300 °C (more pronounced in the EGA data) can be identified for all samples. These peaks can be attributed to the evaporation of organic contaminations possibly introduced during the milling process. This initial weight loss is about 1 %.

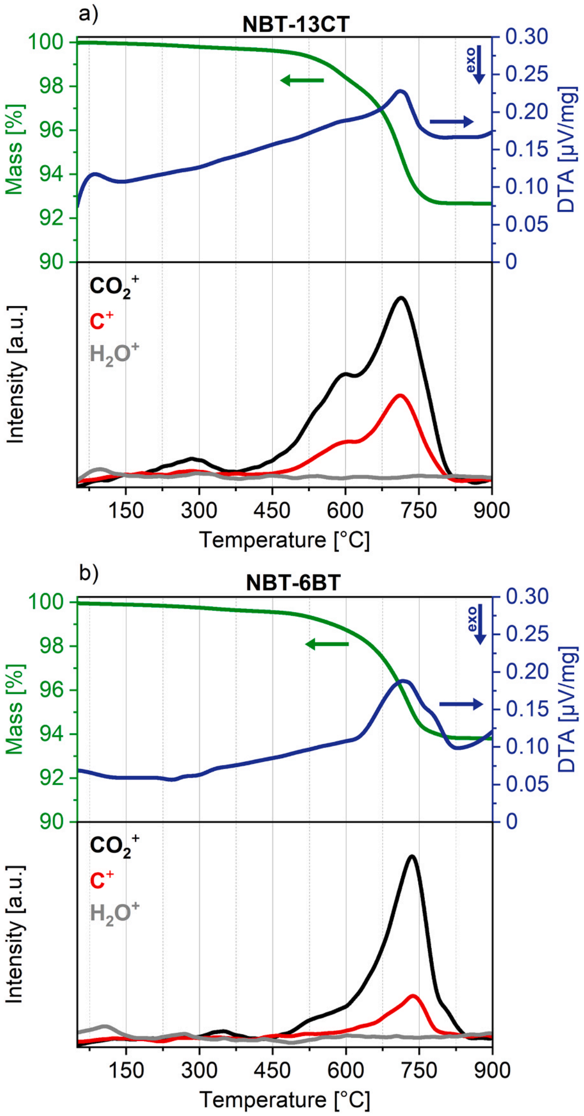

**Fig. 1.** TGA-DTA measurement of the homogenised mixture of starting powders during heating with 5 K/min in air: thermogravimetric analysis (TGA) as well as differential thermal analysis (DTA) (above), and evolved gas analysis EGA (below) for a) NBT–13CT and b) NBT-6BT.

For the samples of the NBT-CT compositions the main weight loss of 7.0 % occurs between 500 °C and 850 °C, which is in agreement with the theoretically calculated value of 7.0 %. This weight loss results from the decomposition of the carbonates and is clearly represented by the strong $CO_2$ peaks in the EGA. The decomposition reactions occur in two clearly separable stages, indicated by two distinct endothermic peaks accompanied by a slope change in the TGA data. Similar to NBT-ST, the first stage of decomposition starts at 450 °C and takes place at around 590 °C. This behaviour can be attributed to the reaction of the raw powder components of NBT that starts at 450 °C and afterwards develops the first perovskite phase [40]. In contrast, the second stage reaction starts about 80 °C earlier at 714 °C and is associated with the formation of CT [42].

With respect to the NBT-BT compositions, the major weight loss of 5.7 % occurs in the temperature range of 650 °C to 850 °C and is also the theoretically calculated weight loss. Again, this weight loss results from the decomposition of the carbonates. While the decomposition reaction occurs at two distinct stages for the NBT-ST and NBT-CT compositions, it occurs within one chemical reaction for NBT-BT. There is no change in the slope of the TGA or distinguishable peaks in the DTA data to indicate multiple reactions. Concerning the NBT-BT composition the main peak appears at 733 °C. Hou et al. [43], through their XRD analysis, confirmed that the reaction of NBT-BT occurs within a single reaction step. The onset of the reaction did not change for NBT-9BT or NBT-13BT, indicating that the behaviour is characteristic for the material system. Anyhow, an additional shoulder at around 780 °C can be observed and correlated with the onset of the phase transition of some left-over $BaCO_3$ from the orthorhombic to hexagonal phase [44].

Clear differences can be seen between NBT-BT, NBT-CT, and the reference system NBT-ST. Since the formation behaviours of the MPB and 25 mol% compositions are consistent (compare Figure S1), the influence of varying amounts of CT, BT, and ST can be ruled out. All differences are, therefore, due to the choice of the material system. In a previous work [14], we already discussed the highly complex diffusion mechanisms in NBT-ST, providing evidence for $Sr^{2+}$ and $O^{2-}$ being the key diffusion partners. Nevertheless, this may not necessarily apply to other solid solutions, as the differences in the formation behaviour could also arise due to different solubilities, crystal structures, or Gibbs Free Energies of mixing of the different titanates in NBT. Modelling the atomic interactions on the electronic level by performing a first-principles approach using Density Functional Theory (DFT) could help to predict phase stabilities as well as boundaries and miscibility gaps, but is beyond the scope of this work.

To ensure the phase purity of each sample, XRD measurements were performed on the sintered and polished pellets before further analysis. The summarised results are depicted in the supplementary material in Figure S2 and demonstrate that each composition consists of a single and pure perovskite phase except for the NBT-CT. It shows minor reflections belonging to the orthorhombic perovskite phase of CT. Anyhow, these reflections are most likely attributed to the core-shell microstructure, still allowing the exclusion of any influence from additional secondary phases.

The effect of the different reaction processes on the evolution of the microstructure as well as on the core-shell formation, is illustrated in the SEM micrographs in Fig. 2 and the characteristic values are summarised in Fig. 3. Referring to the reference composition NBT-25ST, the cores consist of NBT, while the shell is enriched with ST [10,13]. Due to the heavy element bismuth the NBT-cores appear brighter in the BSE images. Core-shell structures can be localised in all three NBT-ST samples (marked with white arrows). However, the core density, which represents the number of cores # per $\mu m^2$, is the highest within the excess composition with 0.569 $\#/\mu m^2$. The core densities of the stoichiometric, approximately 0.002 $\#/\mu m^2$, and the depleted, with about 0.008 $\#/\mu m^2$,

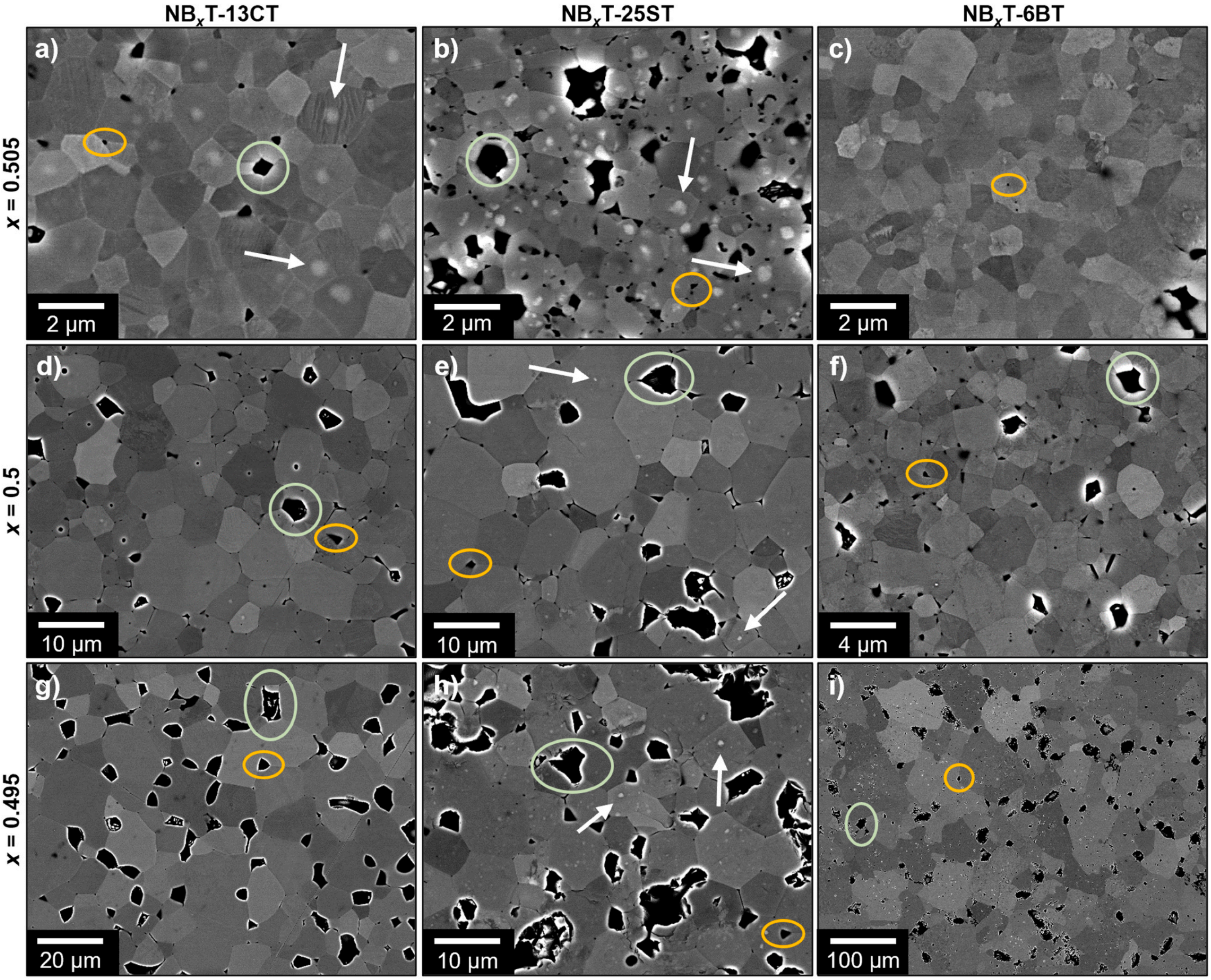

**Fig. 2.** BSE images displaying the evolution of the microstructure of sintered samples prepared with different contents of bismuth $x = 0.495$, 0.5, 0.505 (from bottom to top) for NBT-CT (left side), NBT-ST (middle) and NBT-BT (right side). Cores are marked by white arrows. Pores (orange circles) and break-outs (light green circles) due to sample polishing are marked exemplarily.

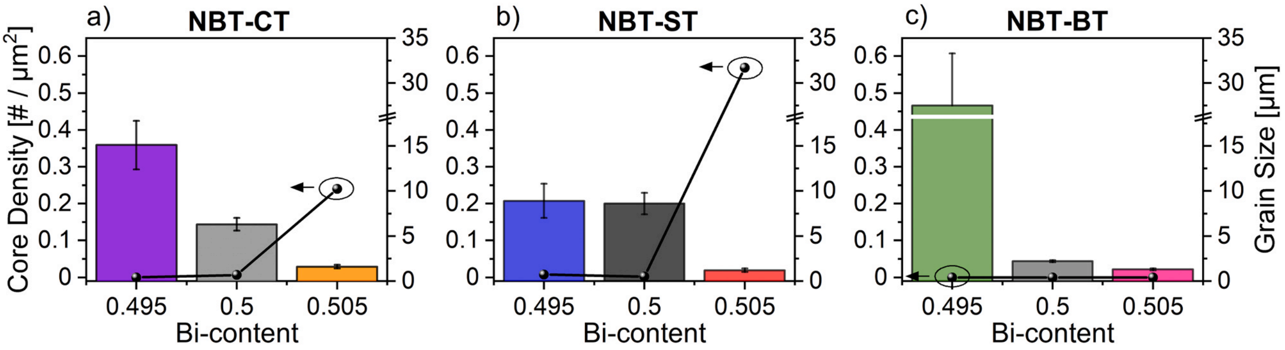

**Fig. 3.** Development of grain size (bar chart) in µm and core density (line plot) in #/µm$^2$ of NBT-CT in a), NBT-ST in b), and NBT-BT in c).

samples are significantly lower. Comparing the core-shell development of NBT-CT with NBT-ST, it is clear that both follow the same trend. The highest core density of 0.240 #/µm$^2$ appears within the excess composition. Nonetheless, the core density is 58 % lower than in NBT-ST. These differences could arise due to the different amounts of CT (13 mol%) and ST (25 mol%) present in the respective MPB compositions. The stoichiometric and depleted samples exhibit very little or even no core-shell structures. In contrast to the results of the NBT-CT compositions, no core-shell structures can be detected within any of the NBT-BT compositions.

Besides the core densities there are also significant variations in the grain size and pore formation. In this regard it needs to be distinguished between pores (orange) and break-outs (light green). The latter appears due to the sample preparation during the polishing steps. All three, NBT-ST, NBT-CT and NBT-BT, show the smallest grain sizes of approximately 1.2 ± 0.2 μm, 1.6 ± 0.2 μm, and 1.3 ± 0.1 μm, for their excess samples. This decrease in grain size as well as low amounts of pores can be attributed to the increased bismuth content, as bismuth acts as a sintering aid and is well-known to affect grain size and pore formation [29,45,46]. On the contrary, the stoichiometric and depleted samples of each solid solution are less comparable. While the grain sizes of the stoichiometric and depleted samples of NBT-ST are quite similar at approximately 8.9 ± 1.9 μm, both NBT-CT and NBT-BT showed a drastic increase of 6.3 ± 0.7 μm to 15.1 ± 2.7 μm and 2.2 ± 0.1 μm to 27.5 ± 5.8 μm, respectively, when comparing the stoichiometric and the depleted compositions. Apart from the significant differences regarding the core-shell formation within the different compositions, the sensitivity of the grain size evolution towards the concentration of oxygen vacancies seems to be strongly dependent on the type of solid solution as well. Still, the overall trends of the increase in grain size with the rise of the oxygen vacancy concentration are consistent for all three solid solutions.

Based on the TGA/DTA/EGA and SEM results, it can be stated, that a decoupling of the formation processes of NBT and the second titanate is a necessary condition for the formation of core-shell structures. In addition to the necessity of a two-step process, oxygen vacancies could be shown to be an additional key factor [13]. A reduction in the oxygen vacancy concentration hinders the chemical diffusion of $Sr^{2+}$ and $O^{2-}$ or $Ca^{2+}$ and $O^{2-}$, respectively. Thus, chemical inhomogeneities like core-shell structures are more likely to form in the excess samples leading to a higher core density here. The condition of a two-step reaction has to be fulfilled before oxygen vacancies can be used to effectively regulate the chemical diffusion and the final number of core-shell structures. As a result, controlling the concentration of oxygen vacancies helped to regulate the number of core-shell structures in NBT-ST and NBT-CT, while NBT-BT still failed to develop any.

### 3.2. *Influence of core-shell microstructures on the electrical properties*

Chemical inhomogeneities like core-shell structures and their effect on the material's properties have only been demonstrated and discussed for the solid solution of NBT and ST so far [10,11,13,14]. The presence of core-shell structures in this specific material system resulted in a non-ergodic NBT core and an ergodic ST-enriched shell. So far, it is expected that the changes within the electromechanical properties, such as a slimming and pinching of the polarisation loop and a drastic increase in the strain values, are a result of a reversible field-induced phase transition from a polar to a non-polar phase in the non-ergodic core, which can stabilise a ferroelectric phase. Nevertheless, it remains unclear whether these chemical inhomogeneities in the form of core-shell structures are solely responsible for the observed property changes or whether nanoscale phenomena, such as polar nanoregions, could also explain the behaviour. The previous section revealed significant microstructural differences depending on the formation process of each solid solution. To answer the underlying question whether certain property changes are at least correlated to the presence of core-shell structures, a detailed investigation of the ferroelectric and electrical properties is required.

The polarisation and strain response as a function of an externally applied electric field are depicted in Fig. 4 and the derived values are summarised in Table S1. The NBT-ST and the NBT-BT compositions exhibit fully saturated loops at an electrical field of 5 kV/mm. Much higher fields of 13 kV/mm were required to obtain saturated hysteresis curves of the NBT-CT compositions. In this context, it should be noted that values such as maximum strain and saturation polarisation scale with the magnitude of the applied electric field. The differences in the electric field required to induce domain switching in NBT-CT may be attributed to the presence of $Ca^{2+}$-ions that could inhibit domain switching. Yuan et al. [47] have already observed similar effects by synthesising (100-$x$)NBT- $x$CT.

Considering that the grain size in all three solid-solutions was drastically altered by changing bismuth content, one could assume that the ferroelectric properties could be affected, as previously reported [48–51]. Since all excess samples display similar grain sizes, the same effect on the properties would be expected. However, significant variations in the shape of the polarisation loops are observed exclusively in the NBT-ST and NBT-CT samples, suggesting that grain size is unlikely to be the primary factor responsible for these changes. Apart from the

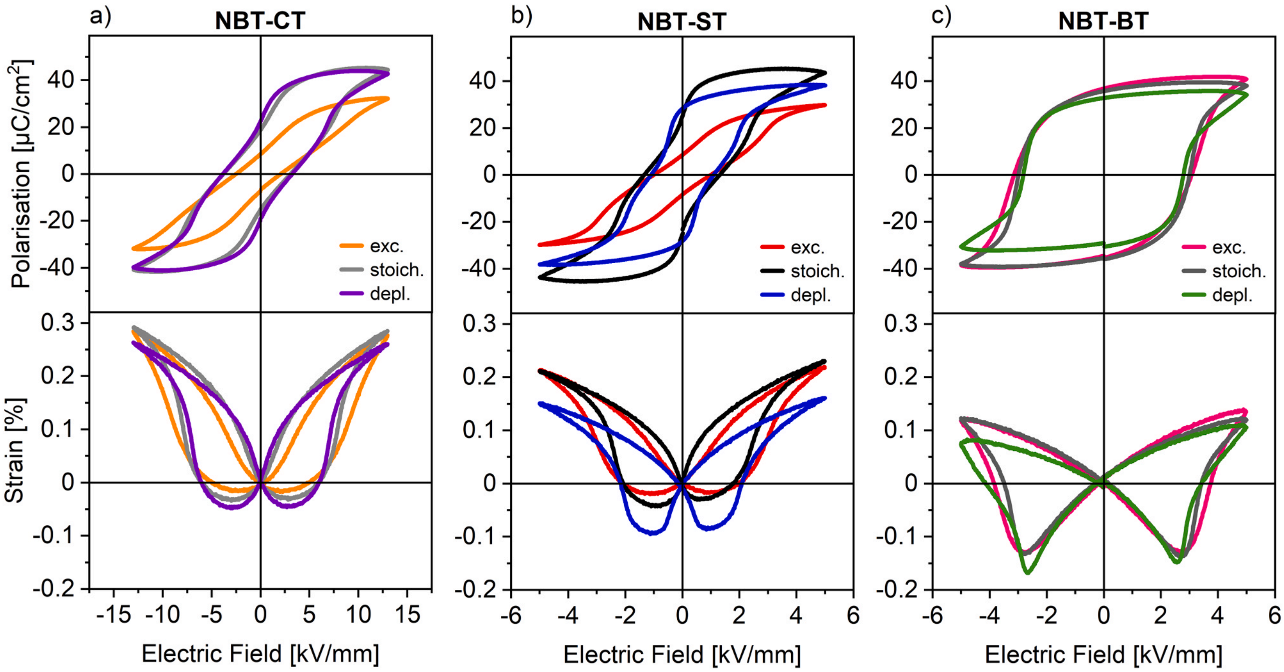

**Fig. 4.** 3rd loop of the bipolar polarisation and strain response versus electric field for a) NBT-13CT, b) NBT-25ST, and c) NBT-6BT measured at 1 Hz. Each graph contains plots of the excess (orange, red, and pink), the stoichiometric (light grey, black, and dark grey), and the depleted (purple, blue, and green) compositions.

variations in grain size, core-shell structures (Fig. 2) developed only within the NBT-ST and NBT-CT compositions. Consequently, it is more likely that the property changes result from inhomogeneities in the composition that only formed in the solid solutions with ST and CT.

Although the NBT-CT and NBT-ST samples both develop core-shell structures causing a similar behaviour of the polarisation and strain responses, it is noteworthy that the differences within the responses of each the depleted, stoichiometric, and excess sample of NBT-CT are less pronounced compared to the NBT-ST samples. The excess samples show the lowest saturation polarisation, remanent polarisation, and coercive field, indicating relaxor-like behaviour. This is also demonstrated within the strain loops, which exhibit the lowest negative strain. In contrast, quite high maximum strains of 0.29 % (NBT-CT) and 0.22 % (NBT-ST) can be generated. Especially, for the CT composition, strain values have never been reported, as the primary focus so far has been on energy storage applications [26,52–54]. In contrast to the relaxor-like behaviour of the excess compositions, the stoichiometric and depleted compositions shift towards a ferroelectric behaviour. This can be observed by a higher remanent polarisation and coercive field. These changes are accompanied by the fact that the negative strain is much larger, especially for the depleted samples of NBT-ST. Additionally, a correlation of the phase transition field $E_{\text{R-F}}$ with the core density can be observed. The lower the core density of a sample, the lower the transition field $E_{\text{R-F}}$ and the phase transition occurs more abruptly as the increase of polarisation and strain are steeper at the $E_{\text{R-F}}$ (Figure S3 in the supplementary material). This behaviour has been discussed previously, particularly for the NBT-ST composition [10–12]. If a sample does not exhibit core shell structures, each grain is homogeneous. When an external electric field is applied, it is uniformly distributed. This leads to an immediate electric field-induced phase transition and a significant change in polarisation at the transition field $E_{\text{R-F}}$. In contrast, core-shell samples exhibit inhomogeneities within almost every grain, namely the NBT-rich and the ST or CT-enriched shell. According to the different permittivities of the non-ergodic core and the ergodic shell, and in order to maintain the polarisation coupling between them, the distribution of the local electric field is broadened. As a result, the increase in polarisation at the transition field $E_{\text{R-F}}$ is less pronounced. A similar behaviour is observed when measuring the current density of the poled samples against temperature. The peak related to the ferroelectric-to-realxor transition temperature $T_{\text{F-R}}$ appears broad and less pronounced indicating no sharp phase transition (Figure S4 and the derived values in Table S1).

In contrast to the core-shell compositions, NBT-BT presents a completely different behaviour. Independent of the bismuth content all three samples feature a typical ferroelectric response with large remanent polarisation and coercive field, that is, a rectangular hysteresis loop, which agrees well with the literature [29]. These findings in the polarisation loops are supported by the current density measurements of poled samples against temperature that show a ferroelectric-to-relaxor transition temperature $T_{\text{F-R}}$ far above room temperature at around 100 °C (Figure S4 and the derived values in Table S1). The positive strains are lowest among all solid solutions, around 0.11 %, while the negative strains are more pronounced, approximately at -0.13 %.

The analysis of the ferroelectric properties reveals a clear correlation between the presence of chemical inhomogeneities – deliberately introduced by controlling the defect chemistry of each solid solution by adjusting the bismuth content, and consequently oxygen vacancy concentration – and changes in material behaviour. A slimming and pinching of the polarisation loops, as well as the appearance of relatively large maximum strains were observed in all samples exhibiting such chemical inhomogeneities. However, nanoscale inhomogeneities in the form of polar nanoregions may also contribute to these effects and should be further investigated in an additional in-depth study.

Previous impedance studies of NBT-based compositions have revealed that higher concentrations of oxygen vacancies lead to increased conductivity values and a transition from electronic towards oxygen ionic conduction [29,55]. This was clearly demonstrated by a rise in the conductivity values by several orders of magnitude and drastic changes in the activation energies when comparing NBT-based samples with and without acceptor-doping of Fe [55] or different bismuth contents [29]. This unique feature of marginally changing the oxygen vacancy concentration and thereby controlling the ionic conductivity can be used to tune the electrical properties of NBT-based materials thoroughly. It is anticipated that these drastic effects of the oxygen vacancy concentration could provide valuable insights into the mobility of different ions during the calcination of NBT-based solid solutions such as NBT-ST, NBT-CT, and NBT-BT, potentially linking these effects to phenomena like the core-shell structure formation. Therefore, Arrhenius plots (Fig. 5d)-f)) of the conductivity have been extracted from the Nyquist plots (Fig. 5a)-c)) following the Arrhenius law, to evaluate the electrical properties in dependence of temperature and frequency (Table S2).

As observed within the previous NBT-based studies, the resistivity changes considerably when the bismuth content and, in turn, oxygen vacancy concentration are varied (compare Eq. (1)). It can be clearly distinguished between samples with lower (excess compositions) and higher oxygen vacancy concentrations (depleted and stoichiometric compositions). Apart from that, clear differences depending on the type of solid solution and, in turn, corresponding ions occupying the *A*-site can be determined.

All excess samples – independent of the solid solution type – exhibit high resistances. Consequently, the Arrhenius plots feature the overall lowest conductivity of $10^{-8}$ S/cm at 500 °C. The activation energies $E_a$ calculated based on the slopes of the Arrhenius plots of NBT-CT, NBT-ST, and NBT-BT are 1.55 eV, 1.71 eV, and 1.48 eV, respectively. According to literature, the bandgaps $E_g$ of pure NBT, CT, ST, and BT, are 3.3 eV [56], 3.46 eV [57], 3.25 eV [58], and 3.20 eV [59], respectively, indicating that the band gap of the corresponding solid solutions should be around 3.2–3.5 eV. The calculated activation energies align well with the theoretical values from the literature, where $E_g \sim 2E_a$ suggests that intrinsic electronic conduction is occurring [56]. The stoichiometric NBT-BT sample features a similar behaviour, which might indicate that the variation in the amount of oxygen vacancies is insufficient to cause a drastic increase in conductivity. All samples that exhibit high resistances and an intrinsic electronic conduction additionally show low tan($\delta$) values over a broad temperature range (Figure S4).

As expected, significantly higher conductivities of about $10^{-7}$ S/cm to even $10^{-5}$ S/cm at 500 °C can be observed for the stoichiometric NBT-CT and NBT-ST as well as all depleted samples that should contain a substantially larger amount of oxygen vacancies compared to the excess compositions. Nevertheless, significant differences depending on the type of solid solution occur. NBT-CT seems to be less sensitive towards the effect of oxygen vacancies as the conductivity only increases by one order of magnitude compared to the excess sample. Additionally, no change towards a dominating oxygen ionic conduction can be observed, as the increase of the activation energy from $E_a \sim 1.05$ eV towards $E_a \sim 1.45$ eV with increasing temperature, more likely indicates a change from extrinsic to intrinsic semiconducting behaviour [60]. Both the rather small increase in conductivity as well as no hint towards a dominating oxygen ionic conduction mechanism, limit the capability of tuning the electrical properties like observed in other NBT-based materials before [13,29]. In contrast, NBT-ST and NBT-BT are strongly affected by the change in the oxygen vacancy concentration. Both show a drastic increase in the conductivity by two to even three orders of magnitude. Moreover, clear evidence of a change towards a dominating ionic conduction mechanism can be observed. First, the activation energies of $E_a \sim 0.75$ eV and $E_a \sim 0.80$ eV are similar to previous results in the literature that have been related to oxygen ionic conduction [13,29,61]. Second, a Warburg-type diffusion, that appears as a linear response with a phase angle of 45° at low frequencies in the Nyquist plot can be detected and hints towards oxygen accumulating at the interface of electrode and ceramic [62,63].

Although it has been demonstrated that the oxygen vacancy

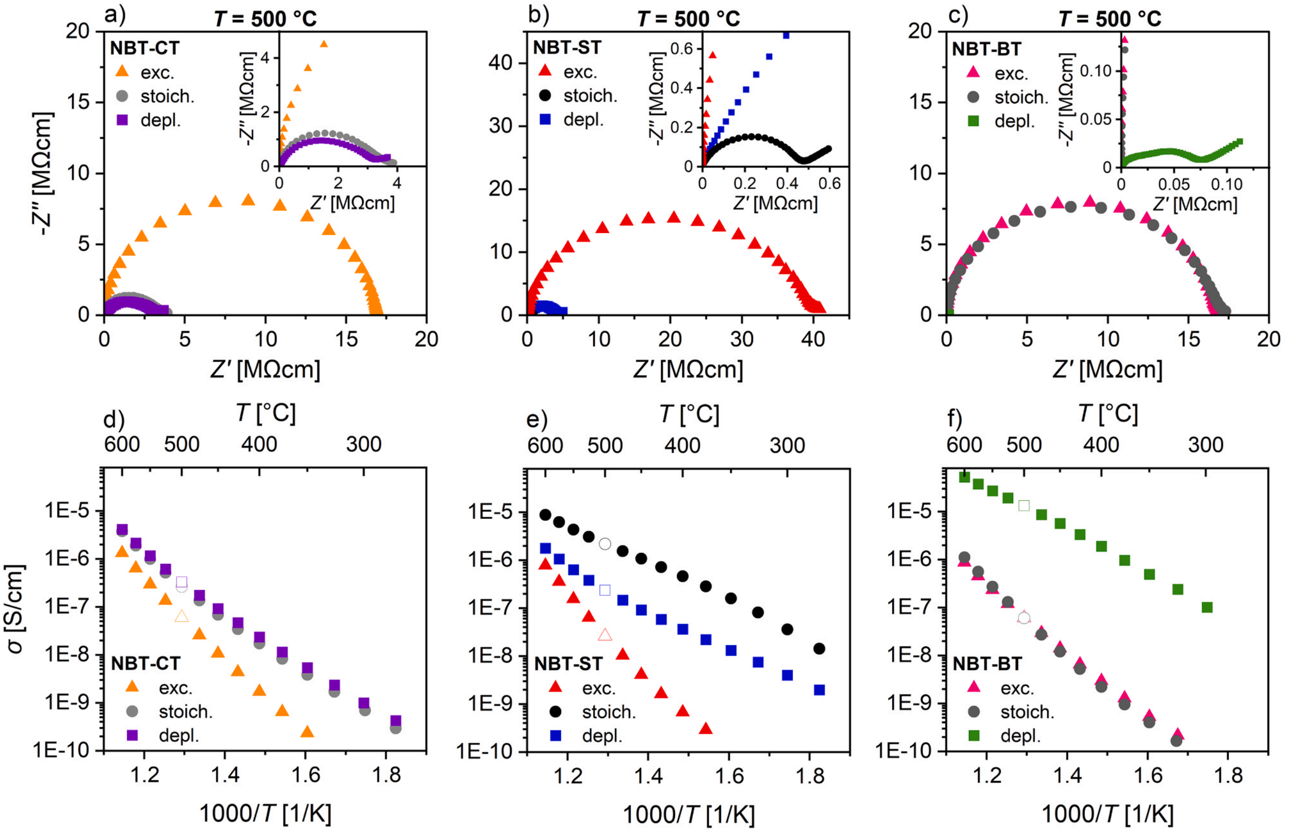

**Fig. 5.** In a)-c) exemplary Nyquist plots measured at 500 °C with NBT-13CT in a), NBT-25ST in b), and NBT-6BT in c). In d)-e) corresponding Arrhenius plots of a) NBT-13CT, b) NBT-25ST, and c) NBT-6BT. The data points at 500 °C that belong to the Nyquist plots in a)-c) are highlighted by empty circles, squares and triangles. Each material system includes data of the Bi-depleted, stoichiometric, and Bi-excess samples.

concentration clearly influences the resulting conduction mechanisms, and various solid solutions exhibit significantly different sensitivities to the present oxygen vacancy concentrations, precise quantification of mobility and diffusion properties during calcination remains challenging and should be addressed in future research. However, it is still more than likely that the oxygen vacancy concentration and mobility are the keys to controlling the core-shell development [13]. It seems to impact the chemical diffusion process involved in core-shell formation significantly.

Other than for the ferroelectric properties, the property changes observed in the electrical analysis cannot clearly be correlated with the presence of core-shell structures, but rather to the presence of oxygen vacancies and the sensitivity of each solid solution towards them. Both ferroelectric and electrical properties emphasise the importance of a precise stoichiometry control, as the oxygen vacancies concentration strongly affects the microstructure, the formation of core-shell structures and the resulting polarisation and strain behaviour. Furthermore, the dominant conduction mechanisms and conductivity values can be substantially modified.

## 4. Conclusion

This work directly correlates the *A*-site ion variation and the present oxygen vacancy concentration through bismuth off-stoichiometry with the reaction pathways during solid-state synthesis of NBT-25ST, NBT-13CT, and NBT-6BT. These changes in reaction pathways lead to significant differences in microstructure and core-shell formation, which, in turn, have a remarkable impact on the ferroelectric and electrical properties.

By means of thermal analysis, it was found that NBT-13CT forms via two separate reactions, the same as observed in NBT-ST before. In both systems, the NBT phase forms first at 590 °C, followed by the formation of CT at 714 °C or ST at 800 °C. In contrast, the reaction of NBT-BT takes place within one single step at 730 °C. This decoupling of the formation of NBT and the second titanate is necessary for the core-shell formation. The variation of bismuth stoichiometry allows the effective regulation of oxygen vacancy concentration, thereby controlling the chemical diffusion of Ca$^{2+}$/Sr$^{2+}$ and O$^{2-}$ and the final core density. In the case of bismuth-excess samples of NBT-CT and NBT-ST, the highest core densities are formed. A high core density stabilises a relaxor-like behaviour, leading to a low remanent polarisation as well as coercive field, a broadened phase transition with enhanced $E_{\text{R-F}}$, and high strains. Remarkably, a maximum strain of 0.29 % is obtained for NBT-CT, the largest ever reported for such composition. In contrast, NBT-BT without core-shell structures exhibits a ferroelectric-like polarisation and strain response unaffected by bismuth content. The electrical properties are less influenced by the core-shell structure but rather by the presence of oxygen vacancies. A low intrinsic electronic conductivity of $10^{-8}$ S/cm at 500 °C is observed in all bismuth-excess samples with a low oxygen vacancy concentration. In contrast, higher vacancy concentrations in the stoichiometric and depleted samples resulted in a drastic increase in the conductivity values up to three orders of magnitude accompanied by a shift towards oxygen ionic conduction.

The results emphasise the importance of controlling stoichiometry and reaction pathways to tailor properties to specific application requirements. Future research should address the challenging yet essential task of quantifying mobility and diffusion properties during calcination.

## CRediT authorship contribution statement

**Till Frömling:** Writing – review & editing, Supervision, Resources, Project administration, Funding acquisition, Conceptualization. **Marc**

**Widenmeyer:** Writing – review & editing, Investigation, Formal analysis. **Sophie Bauer:** Writing – review & editing, Writing – original draft, Visualization, Validation, Methodology, Investigation, Formal analysis, Conceptualization.

## Declaration of Competing Interest

The authors declare that they have no known competing financial interests or personal relationships that could have appeared to influence the work reported in this paper.

## Acknowledgements

Sophie Bauer and Till Frömling gratefully acknowledge the financial support by the Deutsche Forschungsgemeinschaft (DFG, German Research Foundation; Project-ID 471260201). Marc Widenmeyer kindly acknowledges the funding provided by the Deutsche Forschungsgemeinschaft (DFG, German Research Foundation; Project-ID 463184206) within SFB 1548. Special thanks to Leonie Frohnapfel and Dr. Enrico Bruder (Physical Metallurgy, TU Darmstadt, Germany) for their help with the SEM images.

## Appendix A. Supporting information

Supplementary data associated with this article can be found in the online version at doi:10.1016/j.jeurceramsoc.2025.117588.

## References

[1] J. Rödel, W. Jo, K.T.P. Seifert, E.-M. Anton, T. Granzow, D. Damjanovic, Perspective on the development of lead-free piezoceramics, J. Am. Ceram. Soc. 92 (6) (2009) 1153–1177, https://doi.org/10.1111/j.1551-2916.2009.03061.x.

[2] J. Buzek, E. Győri, Directive 2011/65/EU on restriction of the use of certain hazardous substances in electrical and electronic equipment, Eur. Parlim. Counc. Strasbg. (2011).

[3] J. Rödel, K.G. Webber, R. Dittmer, W. Jo, M. Kimura, D. Damjanovic, Transferring lead-free piezoelectric ceramics into application, J. Eur. Ceram. Soc. 35 (6) (2015) 1659–1681, https://doi.org/10.1016/j.jeurceramsoc.2014.12.013.

[4] X. Lv, X. Wang, Y. Ma, X. Zhang, J. Wu, Temperature stability of perovskite-structured lead-free piezoceramics: evaluation methods, improvement strategies, and future perspectives, Mater. Sci. Eng. R. Rep. 159 (2024) 100793, https://doi.org/10.1016/j.mser.2024.100793.

[5] L. Cangini, et al., Hardening of K$_{0.5}$Na$_{0.5}$NbO$_3$ piezoceramics with Cu and the temperature dependence in high-power drive, J. Mater. 11 (3) (2025) 100962, https://doi.org/10.1016/j.jmat.2024.100962.

[6] M. Gehringer, A.-P. Hoang, L. Fulanović, K. Makarovič, B. Malič, T. Frömling, Prototyping Na$_{0.5}$Bi$_{0.5}$TiO$_3$-based multilayer ceramic capacitors for high-temperature and power electronics, J. Eur. Ceram. Soc. 43 (14) (2023) 6122–6129, https://doi.org/10.1016/j.jeurceramsoc.2023.06.073.

[7] M. Zhou, et al., Induced core–shell structure and the electric properties of (K$_{0.48}$Na$_{0.52}$)0.95Li$_{0.05}$Nb$_{0.95}$Sb$_{0.05}$O$_3$ ceramics, Phys. Chem. Chem. Phys. 19 (3) (2017) 1868–1874, https://doi.org/10.1039/C6CP06111G.

[8] H.-C. Thong, C. Zhao, Z.-X. Zhu, X. Chen, J.-F. Li, K. Wang, The impact of chemical heterogeneity in lead-free (K, Na)NbO$_3$ piezoelectric perovskite: ferroelectric phase coexistence, Acta Mater. 166 (2019) 551–559, https://doi.org/10.1016/j.actamat.2019.01.012.

[9] R. Chen, et al., Enhancing core–rim structure control in (K,Na)NbO$_3$-based lead-free piezoceramics via rapid sintering method, J. Eur. Ceram. Soc. 44 (7) (2024) 4612–4621, https://doi.org/10.1016/j.jeurceramsoc.2024.01.084.

[10] J. Koruza, et al., Formation of the core–shell microstructure in lead-free Bi$_{1/2}$Na$_{1/2}$TiO$_3$-SrTiO$_3$ piezoceramics and its influence on the electromechanical properties, J. Eur. Ceram. Soc. 36 (4) (2016) 1009–1016, https://doi.org/10.1016/j.jeurceramsoc.2015.11.046.

[11] M. Acosta, et al., Core–shell lead–free piezoelectric ceramics: current status and advanced characterization of the Bi$_{1/2}$Na$_{1/2}$TiO$_3$–SrTiO$_3$ system, J. Am. Ceram. Soc. 98 (11) (2015) 3405–3422, https://doi.org/10.1111/jace.13853.

[12] N. Liu, M. Acosta, S. Wang, B.-X. Xu, R.W. Stark, C. Dietz, Revealing the core-shell interactions of a giant strain relaxor ferroelectric 0.75Bi$_{1/2}$Na$_{1/2}$TiO$_3$-0.25SrTiO$_3$, Sci. Rep. 6 (1) (2016) 36910, https://doi.org/10.1038/srep36910.

[13] S. Steiner, J. Heldt, O. Sobol, W. Unger, T. Frömling, Influence of oxygen vacancies on core-shell formation in solid solutions of (Na,Bi)TiO$_3$ and SrTiO$_3$, J. Am. Ceram. Soc. 104 (9) (2021) 4341–4350, https://doi.org/10.1111/jace.17845.

[14] T. Frömling, et al., Designing properties of (Na$_{1/2}$Bi$_x$)TiO$_3$-based materials through A-site non-stoichiometry, J. Mater. Chem. C. 6 (4) (2018) 738–744, https://doi.org/10.1039/C7TC03975A.

[15] X. Zhou, et al., Lead-free ferroelectrics with giant unipolar strain for high-precision actuators, Nat. Commun. 15 (1) (2024) 6625, https://doi.org/10.1038/s41467-024-51082-6.

[16] L. Molina-Luna, et al., Enabling nanoscale flexoelectricity at extreme temperature by tuning cation diffusion, Nat. Commun. 9 (1) (2018) 4445, https://doi.org/10.1038/s41467-018-06959-8.

[17] M. Acosta, W. Jo, J. Rödel, Temperature- and frequency-dependent properties of the 0.75Bi$_{1/2}$Na$_{1/2}$TiO$_3$–0.25SrTiO$_3$ lead-free incipient piezoceramic, J. Am. Ceram. Soc. 97 (6) (2014) 1937–1943, https://doi.org/10.1111/jace.12884.

[18] Y. Hiruma, Y. Imai, Y. Watanabe, H. Nagata, T. Takenaka, Large electrostrain near the phase transition temperature of (Bi$_{0.5}$Na$_{0.5}$)TiO$_3$–SrTiO$_3$ ferroelectric ceramics, Appl. Phys. Lett. 92 (26) (2008) 262904, https://doi.org/10.1063/1.2955533.

[19] S. Dong, Review on piezoelectric, ultrasonic, and magnetoelectric actuators, J. Adv. Dielectr. 02 (01) (2012) 1230001, https://doi.org/10.1142/S2010135X12300010.

[20] M. Saleem, et al., Electromechanical properties of nb doped 0.76Bi$_{0.5}$Na$_{0.5}$TiO$_3$–0.24SrTiO$_3$ ceramic, RSC Adv. 6 (92) (2016) 89210–89220, https://doi.org/10.1039/C6RA14999E.

[21] T.A. Duong, et al., Dielectric and piezoelectric properties of Bi$_{1/2}$Na$_{1/2}$TiO$_3$–SrTiO$_3$ lead–free ceramics, J. Electroceram. 41 (1) (2018) 73–79, https://doi.org/10.1007/s10832-018-0161-y.

[22] H. Qi, T. Hu, S. Deng, H. Liu, Z. Fu, J. Chen, Giant dynamic electromechanical response via field driven pseudo-ergodicity in nonergodic relaxors, Nat. Commun. 14 (1) (2023) 2414, https://doi.org/10.1038/s41467-023-38006-6.

[23] Y. Kang, et al., The understanding of large electromechanical strain under low electric field in lead-free BNT-based relaxor, J. Korean Ceram. Soc. (2024), https://doi.org/10.1007/s43207-024-00451-4.

[24] T. Meng, et al., Enhanced field-induced-strain by maximizing reversible domain switching contribution via eliminating negative strain in (Na$_{0.5}$Bi$_{0.5}$)TiO$_3$-based ceramics, J. Mater. Sci. Mater. Electron 33 (9) (2022) 6802–6815, https://doi.org/10.1007/s10854-022-07857-y.

[25] P. Ge, B. Tian, Z. Hong, M. Liu, S. Yang, X. Ke, Origin of superior energy storage performance in antiferroelectric relaxors, Acta Mater. 286 (2025) 120759, https://doi.org/10.1016/j.actamat.2025.120759.

[26] Z. Jiang, Y. Yuan, H. Yang, E. Li, S. Zhang, Excellent thermal stability and energy storage properties of lead-free Bi$_{0.5}$Na$_{0.5}$TiO$_3$-based ceramic, J. Am. Ceram. Soc. 105 (6) (2022) 4027–4038, https://doi.org/10.1111/jace.18332.

[27] A. Hussain, et al., Electromechanical properties of lead-free Nb-Doped 0.95Bi$_{0.5}$Na$_{0.5}$TiO$_3$-0.05BaZrO$_3$ piezoelectric ceramics, Phys. Status Solidi. 215 (20) (2018) 1700942, https://doi.org/10.1002/pssa.201700942.

[28] A. Maqbool, et al., Enhanced electric field-induced strain and ferroelectric behavior of (Bi$_{0.5}$Na$_{0.5}$)TiO$_3$–BaTiO$_3$–SrZrO$_3$ lead-free ceramics, Ceram. Int. 40 (8) (2014) 11905–11914, https://doi.org/10.1016/j.ceramint.2014.04.026 (Part A).

[29] I.-T. Seo, S. Steiner, T. Frömling, The effect of a site non-stoichiometry on 0.94 (Na$_y$Bi$_x$)TiO$_3$-0.06BaTiO$_3$, J. Eur. Ceram. Soc. 37 (4) (2017) 1429–1436, https://doi.org/10.1016/j.jeurceramsoc.2016.11.045.

[30] R.D. Shannon, C.T. Prewitt, Revised values of effective ionic radii, Acta Crystallogr. Sect. B 26 (7) (1970) 1046–1048, https://doi.org/10.1107/S0567740870003576.

[31] M. Dayah, Ptable - Periodensystem. ⟨https://ptable.com/#Eigenschaften⟩.

[32] T. Takenaka, K.M. Kei-ichi Maruyama, K.S. Koichiro Sakata, Bi$_{1/2}$Na$_{1/2}$)TiO$_3$-BaTiO$_3$ system for Lead-Free piezoelectric ceramics, Jpn. J. Appl. Phys. 30 (9S) (1991) 2236, https://doi.org/10.1143/JJAP.30.2236.

[33] B.-J. Chu, D.-R. Chen, G.-R. Li, Q.-R. Yin, Electrical properties of Na$_{1/2}$Bi$_{1/2}$TiO$_3$–BaTiO$_3$ ceramics, J. Eur. Ceram. Soc. 22 (13) (2002) 2115–2121, https://doi.org/10.1016/S0955-2219(02)00027-4.

[34] R. Roukos, N. Zaiter, D. Chaumont, Relaxor behaviour and phase transition of perovskite ferroelectrics-type complex oxides (1–x)Na$_{0.5}$Bi$_{0.5}$TiO$_3$–xCaTiO$_3$ system, J. Adv. Ceram. 7 (2) (2018) 124–142, https://doi.org/10.1007/s40145-018-0264-6.

[35] R. Roukos, S.A. Dargham, J. Romanos, F. Barakat, D. Chaumont, Complex structural contribution of the morphotropic phase boundary in Na$_{0.5}$Bi$_{0.5}$TiO$_3$ - CaTiO$_3$ system, Ceram. Int. 45 (4) (2019) 4467–4473, https://doi.org/10.1016/j.ceramint.2018.11.126.

[36] R. Roukos, S.A. Dargham, J. Romanos, D. Chaumont, Detection of morphotropic phase boundary in A-site/Ca-substituted Na$_{0.5}$Bi$_{0.5}$TiO$_3$ complex oxides ferroelectric system, J. Alloy. Compd. 840 (2020) 155509, https://doi.org/10.1016/j.jallcom.2020.155509.

[37] S. Sayyed, S.A. Acharya, P. Kautkar, V. Sathe, Structural and dielectric anomalies near the MPB region of Na$_{0.5}$Bi$_{0.5}$TiO$_3$–SrTiO$_3$ solid solution, RSC Adv. 5 (63) (2015) 50644–50654, https://doi.org/10.1039/C5RA05617A.

[38] W.P. Cao, et al., Large electrocaloric response and high energy-storage properties over a broad temperature range in lead-free NBT-ST ceramics, J. Eur. Ceram. Soc. 36 (3) (2016) 593–600, https://doi.org/10.1016/j.jeurceramsoc.2015.10.019.

[39] S. Kim, et al., A correlation between piezoelectric response and crystallographic structural parameter observed in lead-free (1-x)(Bi$_{0.5}$Na$_{0.5}$)TiO$_3$–xSrTiO$_3$ piezoelectrics, J. Eur. Ceram. Soc. 37 (4) (2017) 1379–1386, https://doi.org/10.1016/j.jeurceramsoc.2016.11.023.

[40] T. Kainz, M. Naderer, D. Schütz, O. Fruhwirth, F.A. Mautner, K. Reichmann, Solid state synthesis and sintering of solid solutions of BNT–xBKT, J. Eur. Ceram. Soc. 34 (15) (2014) 3685–3697, https://doi.org/10.1016/j.jeurceramsoc.2014.04.040.

[41] H. Tagawa, K. Kimura, T. Fujino, K. Ouchi, Reactivity of starting materials in formation of strontium titanate, Denki Kagaku oyobi Kogyo Butsuri Kagaku 52 (3) (1984) 154–159, https://doi.org/10.5796/kogyobutsurikagaku.52.154.

[42] V.M. Vukotić, T. Srećković, Z. Marinković, G. Brankovic, M. Cilense, D. Arandjelović, Mechanochemical synthesis of CaTiO$_3$ from CaCO$_3$ - TiO$_2$ mixture,

Mater. Sci. Forum 453–454 (2004) 429–434, https://doi.org/10.4028/www.scientific.net/MSF.453-454.429.

[43] D. Hou, et al., Formation of sodium bismuth titanate—barium titanate during solid-state synthesis, J. Am. Ceram. Soc. 100 (4) (2017) 1330–1338, https://doi.org/10.1111/jace.14631.

[44] S.N. Basahel, E.-H.M. Diefallah, Kinetic analysis of thermal decomposition reactions. Vii. effect of radiation and doping on the thermal decomposition of $BaCO_3$–$TiO_2$ and $SrCO_3$–$TiO_2$ crystalline mixtures, Can. J. Chem. 70 (3) (1992) 888–893, https://doi.org/10.1139/v92-118.

[45] X.X. Wang, X.G. Tang, K.W. Kwok, H.L.W. Chan, C.L. Choy, Effect of excess $Bi_2O_3$ on the electrical properties and microstructure of $(Bi_{1/2}Na_{1/2})TiO_3$ ceramics, Appl. Phys. A 80 (5) (2005) 1071–1075, https://doi.org/10.1007/s00339-003-2350-y.

[46] Y.S. Sung, J.M. Kim, J.H. Cho, T.K. Song, M.H. Kim, T.G. Park, Effects of bi nonstoichiometry in $(Bi_{0.5+x}Na)TiO_3$ ceramics, Appl. Phys. Lett. 98 (1) (2011) 12902, https://doi.org/10.1063/1.3525370.

[47] Y. Yuan, C.J. Zhao, X.H. Zhou, B. Tang, S.R. Zhang, High-temperature stable dielectrics in Mn-modified (1-x) $Bi_{0.5}Na_{0.5}TiO_3$-x$CaTiO_3$ ceramics, J. Electroceram. 25 (2) (2010) 212–217, https://doi.org/10.1007/s10832-010-9617-4.

[48] K. Kinoshita, A. Yamaji, Grain-size effects on dielectric properties in barium titanate ceramics, J. Appl. Phys. 47 (1) (1976) 371–373, https://doi.org/10.1063/1.322330.

[49] C.A. Randall, N. Kim, J.-P. Kucera, W. Cao, T.R. Shrout, Intrinsic and extrinsic size effects in Fine-Grained Morphotropic-Phase-Boundary lead zirconate titanate ceramics, J. Am. Ceram. Soc. 81 (3) (1998) 677–688, https://doi.org/10.1111/j.1151-2916.1998.tb02389.x.

[50] Y. Tan, et al., Unfolding grain size effects in barium titanate ferroelectric ceramics, Sci. Rep. 5 (1) (2015) 9953, https://doi.org/10.1038/srep09953.

[51] Dragan Damjanovic, Ferroelectric, dielectric and piezoelectric properties of ferroelectric thin films and ceramics, Rep. Prog. Phys. 61 (9) (1998) 1267, https://doi.org/10.1088/0034-4885/61/9/002.

[52] X. Su, et al., Large electrocaloric effect over a wide temperature span in lead-free bismuth sodium titanate-based relaxor ferroelectrics, J. Mater. 9 (2) (2023) 289–298, https://doi.org/10.1016/j.jmat.2022.10.005.

[53] F. Chen, et al., Improved dielectric energy storage performance of $Na_{0.5}Bi_{0.5}TiO_3$-based lead-free relaxation ferroelectric ceramics achieved by domain structural regulation and enhanced densification, Ceram. Int. 49 (19) (2023) 31152–31162, https://doi.org/10.1016/j.ceramint.2023.07.061.

[54] L. Yu, et al., Enhanced electrical energy storage performance of Pb-free A-site $La^{3+}$-doped 0.85$Na_{0.5}Bi_{0.5}TiO_3$-0.15$CaTiO_3$ ceramics, Ceram. Int. 46 (18) (2020) 28173–28182, https://doi.org/10.1016/j.ceramint.2020.07.316 (Part A).

[55] S. Steiner, I.-T. Seo, P. Ren, M. Li, D.J. Keeble, T. Frömling, The effect of Fe-acceptor doping on the electrical properties of $Na_{1/2}Bi_{1/2}TiO_3$ and 0.94 $(Na_{1/2}Bi_{1/2})TiO_3$–0.06 $BaTiO_3$, J. Am. Ceram. Soc. 102 (9) (2019) 5295–5304, https://doi.org/10.1111/jace.16401.

[56] M. Li, et al., A family of oxide ion conductors based on the ferroelectric perovskite $Na_{0.5}Bi_{0.5}TiO_3$, Nat. Mater. 13 (1) (2014) 31–35, https://doi.org/10.1038/nmat3782.

[57] U. Balachandran, B. Odekirk, N.G. Eror, Electrical conductivity in calcium titanate, J. Solid State Chem. 41 (2) (1982) 185–194, https://doi.org/10.1016/0022-4596(82)90201-8.

[58] K. van Benthem, C. Elsässer, R.H. French, Bulk electronic structure of $SrTiO_3$: experiment and theory, J. Appl. Phys. 90 (12) (2001) 6156–6164, https://doi.org/10.1063/1.1415766.

[59] G. Panthi, M. Park, Approaches for enhancing the photocatalytic activities of barium titanate: a review, J. Energy Chem. 73 (2022) 160–188, https://doi.org/10.1016/j.jechem.2022.06.023.

[60] A.J. Moulson, J.M. Herbert, Electroceramics - Materials, Properties, Applications, Wiley, Chichester, 2003.

[61] M. Cherry, M.S. Islam, C.R.A. Catlow, Oxygen ion migration in perovskite-type oxides, J. Solid State Chem. 118 (1) (1995) 125–132, https://doi.org/10.1006/jssc.1995.1320.

[62] R.A. Maier, C.A. Randall, Low-Temperature ionic conductivity of an Acceptor-Doped perovskite: I. Impedance of Single-Crystal $SrTiO_3$, J. Am. Ceram. Soc. 99 (10) (2016) 3350–3359, https://doi.org/10.1111/jace.14348.

[63] M. Bag, et al., Kinetics of ion transport in perovskite active layers and its implications for active layer stability, J. Am. Chem. Soc. 137 (40) (2015) 13130–13137, https://doi.org/10.1021/jacs.5b08535.